Article

Approaching the quantum limit in two-dimensional semiconductor contacts

https://doi.org/10.1038/s41586-022-05431-4

Received: 9 March 2022

Accepted: 7 October 2022

Published online: 11 January 2023

Check for updates

Weisheng Li[1,12], Xiaoshu Gong[2,12], Zhihao Yu[1,12], Liang Ma[2,12], Wenjie Sun[3], Si Gao[3,4], Çağıl Köroğlu[5], Wenfeng Wang[1], Lei Liu[1], Taotao Li[1], Hongkai Ning[1], Dongxu Fan[1], Yifei Xu[1], Xuecou Tu[1], Tao Xu[6], Litao Sun[6], Wenhui Wang[2], Junpeng Lu[2], Zhenhua Ni[2], Jia Li[7], Xidong Duan[7], Peng Wang[3], Yuefeng Nie[3], Hao Qiu[1], Yi Shi[1]✉, Eric Pop[5,8,9], Jinlan Wang[2]✉ & Xinran Wang[1,10,11]✉

The development of next-generation electronics requires scaling of channel material thickness down to the two-dimensional limit while maintaining ultralow contact resistance[1,2]. Transition-metal dichalcogenides can sustain transistor scaling to the end of roadmap, but despite a myriad of efforts, the device performance remains contact-limited[3–12]. In particular, the contact resistance has not surpassed that of covalently bonded metal–semiconductor junctions owing to the intrinsic van der Waals gap, and the best contact technologies are facing stability issues[3,7]. Here we push the electrical contact of monolayer molybdenum disulfide close to the quantum limit by hybridization of energy bands with semi-metallic antimony ($01\bar{1}2$) through strong van der Waals interactions. The contacts exhibit a low contact resistance of 42 ohm micrometres and excellent stability at 125 degrees Celsius. Owing to improved contacts, short-channel molybdenum disulfide transistors show current saturation under one-volt drain bias with an on-state current of 1.23 milliamperes per micrometre, an on/off ratio over 10^8 and an intrinsic delay of 74 femtoseconds. These performances outperformed equivalent silicon complementary metal–oxide–semiconductor technologies and satisfied the 2028 roadmap target. We further fabricate large-area device arrays and demonstrate low variability in contact resistance, threshold voltage, subthreshold swing, on/off ratio, on-state current and transconductance[13]. The excellent electrical performance, stability and variability make antimony ($01\bar{1}2$) a promising contact technology for transition-metal-dichalcogenide-based electronics beyond silicon.

Metal–semiconductor (M–S) contacts have essential roles in modern electronics owing to the continuous scaling of device dimensions[14]. In an ideal M–S junction, there is a fundamental quantum limit in the junction contact resistance by assuming ballistic transport of the conducting modes:

$$R_{c,\min} = \frac{h}{2q^2}\sqrt{\frac{\pi}{2n_{2D}}}, \quad (1)$$

where h is Planck's constant, q is the unit charge and n_{2D} is the carrier concentration in the semiconductor. Such ideal M–S contacts have, however, been rarely obtained experimentally owing to the stringent requirement of energy-level alignment (that is, a zero or negative Schottky barrier) and coherence of wavefunctions across the interface without backscattering[15]. The situation is more complicated for van der Waals (vdW) materials such as transition-metal dichalcogenides (TMDs) owing to their dangling-bond-free surface. The existence of a vdW gap introduces an additional tunnel barrier and reduces the charge injection, making typical R_c values several orders of magnitude higher than the quantum limit[15]. Attempts to overcome such a 'contact gap' include edge contacts[16,17], low-work-function metals[18], ultrahigh vacuum evaporation[8], low-energy metal integration[4,6,19], doping[20,21], tunnelling contacts[22,23] and, more recently, semi-metal contacts[7,9,10,24]. These efforts have reduced the R_c to several hundred

[1]National Laboratory of Solid State Microstructures, School of Electronic Science and Engineering and Collaborative Innovation Center of Advanced Microstructures, Nanjing University, Nanjing, China. [2]School of Physics, Southeast University, Nanjing, China. [3]National Laboratory of Solid State Microstructures, Jiangsu Key Laboratory of Artificial Functional Materials, College of Engineering and Applied Sciences and Collaborative Innovation Center of Advanced Microstructures, Nanjing University, Nanjing, China. [4]College of Materials Science and Engineering, Nanjing Tech University, Nanjing, China. [5]Department of Electrical Engineering, Stanford University, Stanford, CA, USA. [6]SEU-FEI Nano-Pico Center, Key Laboratory of MEMS of Ministry of Education, Southeast University, Nanjing, China. [7]Hunan Key Laboratory of Two-Dimensional Materials and State Key Laboratory for Chemo/Biosensing and Chemometrics, College of Chemistry and Chemical Engineering, Hunan University, Changsha, China. [8]Department of Materials Science and Engineering, Stanford University, Stanford, CA, USA. [9]Precourt Institute for Energy, Stanford University, CA, USA. [10] School of Integrated Circuits, Nanjing University, Suzhou, China. [11]Suzhou Laboratory, Suzhou, China. [12]These authors contributed equally: Weisheng Li, Xiaoshu Gong, Zhihao Yu, Liang Ma. ✉e-mail: yshi@nju.edu.cn; jlwang@seu.edu.cn; xrwang@nju.edu.cn

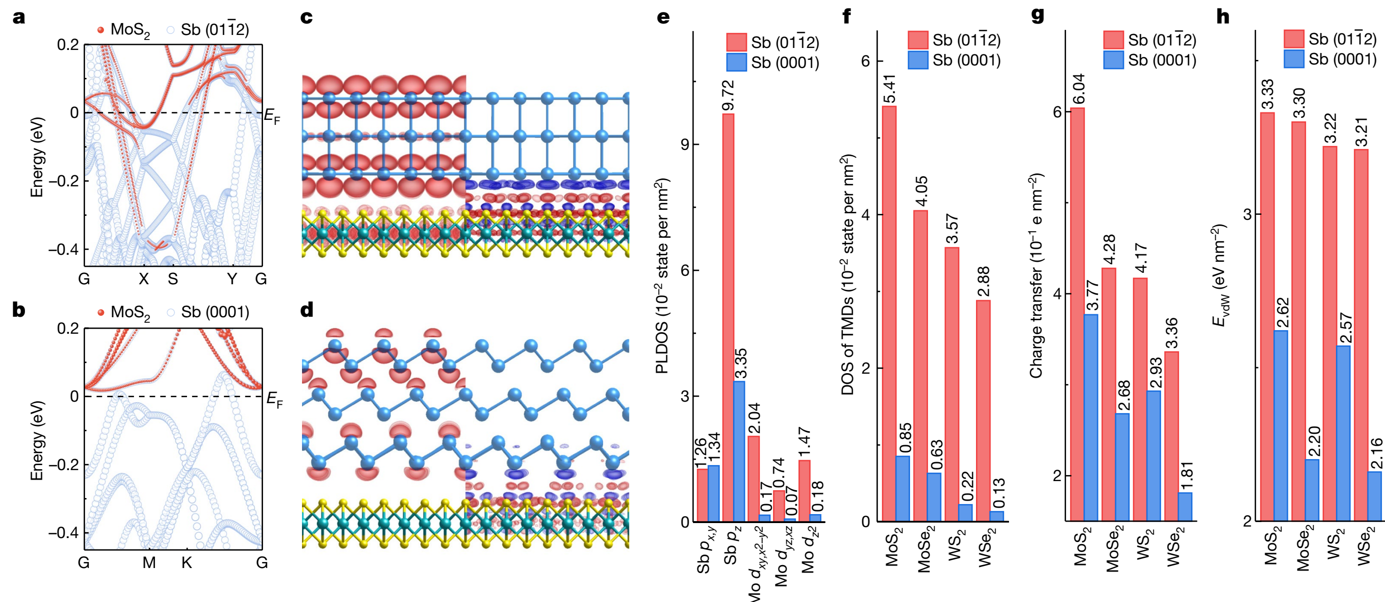

Fig. 1 | Electronic properties of Sb (01$\bar{1}$2)–MoS_2 and Sb (0001)–MoS_2 contacts from DFT calculations. a,**b**, Atomic-projected electronic band structure of Sb (01$\bar{1}$2)–MoS_2 (**a**) and Sb (0001)–MoS_2 (**b**) contacts. The red and blue symbols represent orbitals from MoS_2 and Sb, respectively. The size of the symbols represents the relative contribution. **c**,**d**, The charge density near E_F (left) and the differential charge density (right) of Sb (01$\bar{1}$2) (**c**) and Sb (0001) (**d**) contacts (red, positive; blue, negative). The blue, green and yellow spheres represent Sb, Mo and S atoms, respectively. The differential charge density is calculated by subtracting pre-contact three-layer Sb and MoS_2 charge density from the post-contact charge density. The isosurface level is 9×10^{-5} e Bohr^{-3} and 7×10^{-4} e Bohr^{-3} for the left and right panels, respectively. **e**, Projected PLDOS of different orbitals of Sb (01$\bar{1}$2)–MoS_2 and Sb (0001)–MoS_2 contacts near E_F. **f**, The integrated DOS of TMDs at E_F. **g**, The charge transfer from Sb to TMDs by Bader charge analysis. **h**, The interfacial vdW interaction between TMDs and Sb.

ohm micrometres, which is comparable to but still higher than M–S junctions composed of intimate chemical bonds (for example, doped and undoped silicon (Si) and titanium nitride (TiN)/gallium nitride (GaN)). Besides Schottky barrier height (SBH) and tunnel barrier width, M–S orbital hybridization also has a critical role in the charge injection efficiency[25]. A major limitation of previous studies is that, even for the best semi-metal contacts, the electronic states of M–S remain weakly coupled across the vdW gap[7]. To further reduce R_c, coherent hybridization of M–S energy bands needs to be realized at the Fermi energy (E_F) and across the vdW gap. We note that such hybridized states are within the conduction and valance bands and are spatially delocalized, and are distinct from the localized metal-induced gap states[26,27]. The metal-induced gap states originate from defects and can cause undesirable Fermi level pinning.

Here we realize band hybridization between monolayer molybdenum disulfide (MoS_2) and semi-metallic antimony (Sb) (01$\bar{1}$2). We first use

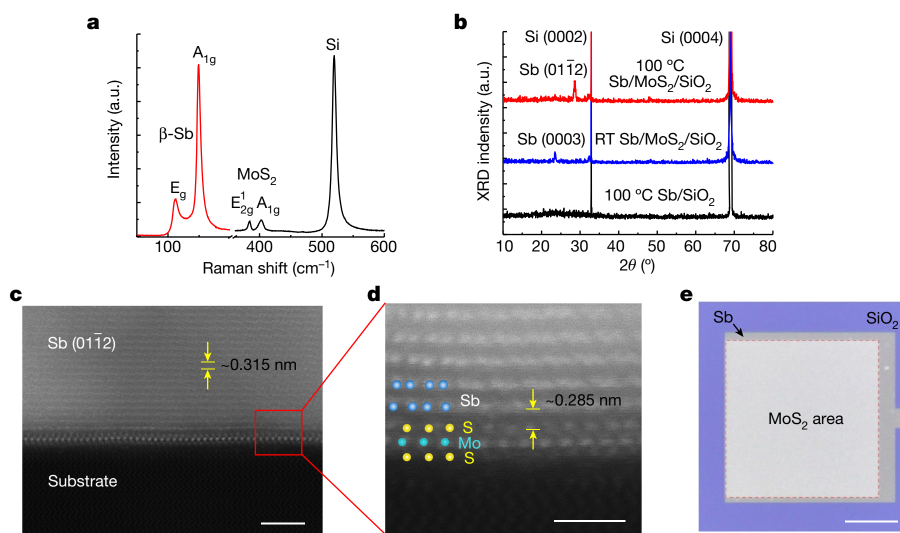

Fig. 2 | Characterization of the Sb (01$\bar{1}$2)–MoS_2 contact. a, Raman spectrum of Sb film deposited on MoS_2/Si substrate shows Sb E_g and A_{1g} peaks at 111 cm^{-1} and 149 cm^{-1}, respectively. **b**, XRD θ–2θ diffractogram of Sb film with different deposition conditions and substrate. RT, room temperature. **c**, Cross-section HAADF-STEM image of the Sb (01$\bar{1}$2)–MoS_2 contact. The interplane distance of 0.315 nm for Sb (01$\bar{1}$2) planes is marked. Scale bar, 2 nm. **d**, Zoom-in atomic-resolution image from the red box in **c**. The Mo, S and Sb atoms are overlayed on the image. The vdW gap of 0.285 nm is marked. Scale bar, 1 nm. **e**, Optical microscope image of Sb films deposited on MoS_2 and SiO_2 substrate, showing clear colour contrast. Scale bar, 20 μm.

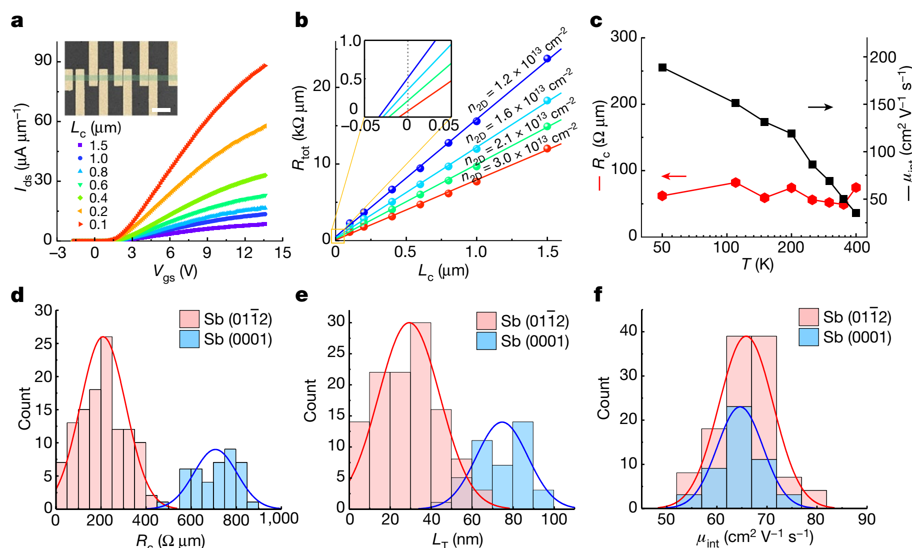

Fig. 3 | Electrical properties and stability of the Sb (01$\bar{1}$2)–MoS$_2$ contact. **a**, Transfer curves of a typical TLM structure with L_c ranging from 0.1 µm to 1.5 µm and V_{ds} = 0.1 V. Inset: false-colour scanning electron microscope image of a TLM structure. Scale bar, 2 µm. **b**, R_c extraction using the TLM method from the device in **a**. From top to bottom, n_{2D} = 1.2 × 10^{13} cm^{-2}, 1.6 × 10^{13} cm^{-2}, 2.1 × 10^{13} cm^{-2} and 3 × 10^{13} cm^{-2}, respectively. Inset: the magnified data plot near L_c = 0, where the y intercept and x intercept represent 2R_c and 2L_T, respectively. It is noted that the L_T derived by the TLM method assumes the same MoS$_2$ sheet resistivity underneath and outside the contact, which is probably violated considering the charge transfer between Sb (01$\bar{1}$2) and MoS$_2$. This could lead to uncertainties in the obtained L_T. **c**. R_c (red squares) and intrinsic mobility (black rhombuses) as a function of temperature for another device. **d**–**f**, R_c (**d**), L_T (**e**) and μ_{int} (**f**) distribution of the Sb (01$\bar{1}$2) and Sb (0001) contacts, respectively. The solid lines are Gaussian fittings.

density-functional theory (DFT) calculations to validate our approach (see Methods for calculation details). Figure 1a,b show the atomically projected band structure of Sb (01$\bar{1}$2)–MoS$_2$ and Sb (0001)–MoS$_2$, respectively. For Sb (01$\bar{1}$2)–MoS$_2$, multiple hybridized bands composed of a molybdenum (Mo) d orbital and Sb p and s orbitals intersect E_F. For Sb (0001)–MoS$_2$, however, the bands intersecting E_F are mainly composed of Sb p and s orbitals, and the MoS$_2$ conduction band minimum is located above E_F (Fig. 1b). To find the origin of band hybridization, we analysed the population of orbitals in the projected local density of states (PLDOS) near E_F (Fig. 1e). It can be seen that, although the Sb $p_{x,y}$ orbitals are comparable, the Sb p_z orbital of Sb (01$\bar{1}$2) is 190% larger than that of Sb (0001) owing to the closely packed atomic surface of Sb (01$\bar{1}$2) (surface Sb atom density, 10.43 nm^{-2} versus 5.34 nm^{-2}). Furthermore, the population of Mo d orbitals in the Sb (01$\bar{1}$2)–MoS$_2$ contact is also markedly enhanced (Fig. 1e). It is noted that the distribution of Sb p_z and Mo d_{z^2} orbitals is mainly along the vertical direction. As a result, a considerable real-space overlap between the Sb p_z orbital and the Mo d orbital emerges (Fig. 1c), which leads to strong band hybridization in the Sb (01$\bar{1}$2)–MoS$_2$ contact. The hybridization is visualized by plotting the spatial charge distribution at E_F in Fig. 1c,d (left). We can see that the charge is distributed in both Sb (01$\bar{1}$2) and MoS$_2$ layers despite the vdW gap, in clear contrast to Sb (0001)–MoS$_2$. We further investigated the charge transfer by calculating the differential charge density as shown in Fig. 1c,d (right). The degree of hybridization and charge transfer was quantified by the integrated DOS of MoS$_2$ at E_F (Fig. 1f) and Bader charge transfer (Fig. 1g). In both cases, the Sb (01$\bar{1}$2)–MoS$_2$ contact shows significant enhancement, which is favourable for M–S contacts. The charge transfer effectively pulls the MoS$_2$ conduction band minimum about 0.4 eV below E_F (Fig. 1a). Therefore, the MoS$_2$ under Sb (01$\bar{1}$2) is degenerated doped and forms ohmic contact with the channel, which is similar to the situation in Si[14]. In fact, the simulated local device density of states (LDDOS) suggest that the band bending across the highly doped contact and the channel region is very steep in real space (about 0.6 nm) and allows considerable carrier tunnelling through this space-charge region in the on state (Extended Data Fig. 1a,b).

We further calculated the interfacial vdW interaction (E_{vdw}) in the heterobilayer. Previous studies have established that the degree of band hybridization in TMD heterostructures can be increased by vdW interaction[28]. Our calculation indeed revealed a strong E_{vdw} = 3.33 eV nm^{-2} for Sb (01$\bar{1}$2)–MoS$_2$, which was much greater than that for Sb (0001)–MoS$_2$ (2.62 eV nm^{-2}; Fig. 1h). This was attributed to the planar instead of protruding distribution of Sb atoms in the (01$\bar{1}$2) plane. We further extended our calculations to several other TMDs (Fig. 1f–h and Extended Data Fig. 2), as well as bismuth (Bi) (01$\bar{1}$2)–MoS$_2$ (Extended Data Fig. 1e–h). In all the cases, the Sb (01$\bar{1}$2) and Bi (01$\bar{1}$2) contacts showed enhanced band hybridization and Bader charge transfer compared with their (0001) counterparts, showing that our approach is general and robust.

Besides band hybridization, another important aspect to realize ohmic contact is the tunnel barrier width. To this end, we calculated the electrostatic potential profile of the contacts (Extended Data Fig. 1c,d). The tunnel barrier width of Sb (01$\bar{1}$2)–MoS$_2$ was 1.35 Å, which was smaller than that of Sb (0001)–MoS$_2$ (1.39 Å) as well as Bi (0001)–MoS$_2$ (1.66 Å) (ref. [7]). This further ensures the low tunnelling resistivity of Sb (01$\bar{1}$2) compared with other semi-metallic contacts.

The evaporation of semi-metals on MoS$_2$ under ambient temperature favoured (0001)-orientated films[7,9,10]. Owing to the enhanced thermodynamic stability (Fig. 1h), we used a mild substrate heating of about 100 °C during evaporation to obtain (01$\bar{1}$2)-oriented Sb films (see Methods for details). Raman spectroscopy (Fig. 2a) revealed that the Sb was semi-metallic β-phase[29]. Figure 2b compares the X-ray diffraction (XRD) θ–2θ (where θ is the X-ray incident angle) diffractograms of Sb deposited on MoS$_2$ under different temperatures. The Sb deposited under ambient temperature showed pronounced (0003) diffraction peak. Under high temperature, however, the (0003) peak almost disappeared and the (01$\bar{1}$2) peak became dominant. Such temperature-dependent orientation was consistent with molecular-beam epitaxy results[30]. The Sb (01$\bar{1}$2) was further confirmed by cross-section high-angle annular dark-field scanning transmission electron microscopy (HAADF-STEM) (Fig. 2c,d). The Sb atomic planes parallel to MoS$_2$ had an interplane distance of 0.315 nm, corresponding to the (01$\bar{1}$2) planes. In contrast, the interplane distance of Sb (0001) was measured to be 0.379 nm

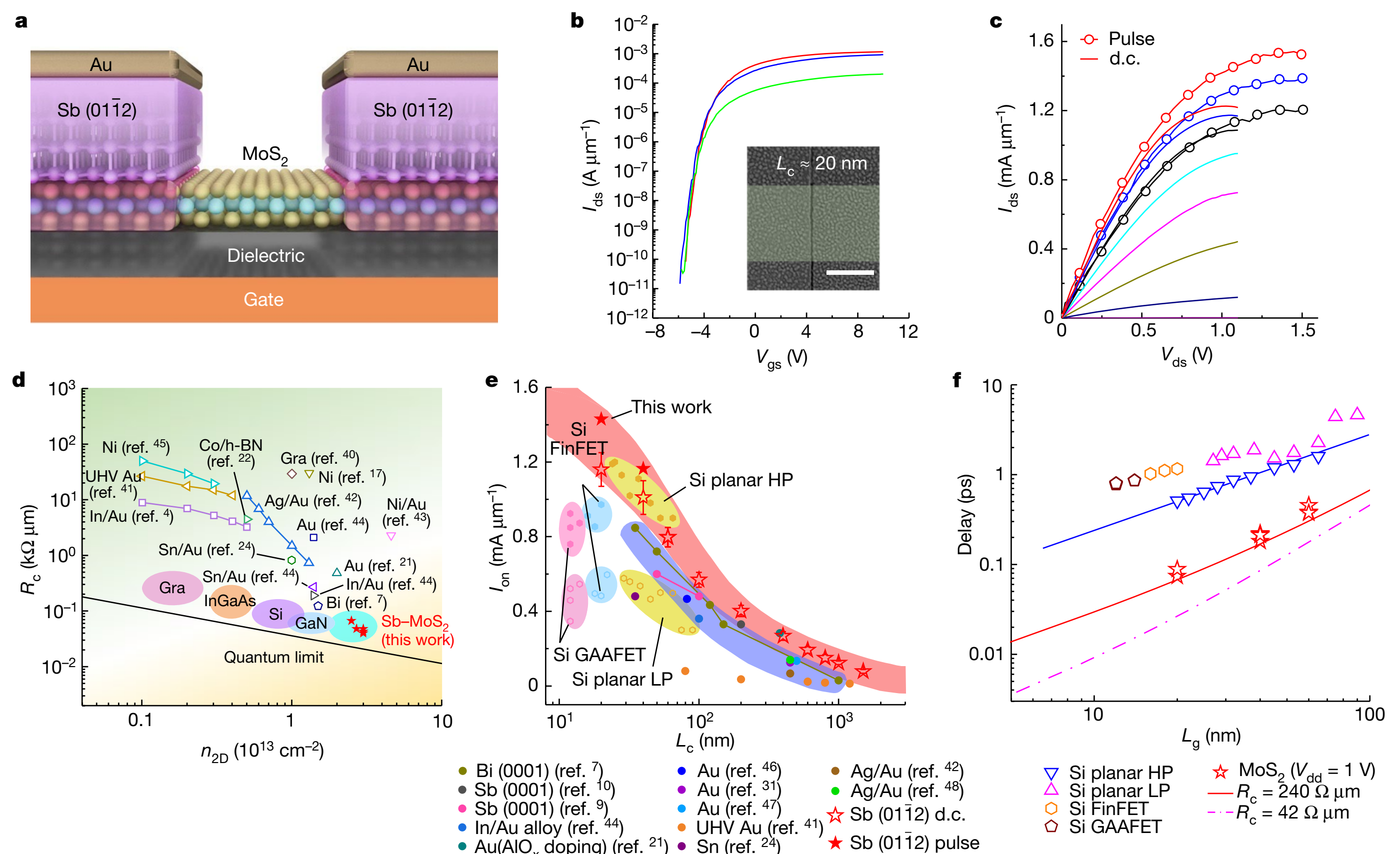

Fig. 4 | Short-channel MoS2 FET performance and benchmark. a, Cartoon illustration of the FET structure. **b**, Transfer characteristics of a typical MoS_2 FET with L_c = 20 nm under V_{ds} = 100 mV (green line), 550 mV (blue line) and 1 V (red line). Inset: false-colour SEM image of the device. Scale bar, 500 nm. **c**, The output characteristics of the same device in **b**. From bottom to top, V_{gs} = −4 V to V_{gs} = 10 V with 2-V steps. The solid and dotted lines are the results of the d.c. and pulse current–voltage measurements, respectively. **d**, R_c as a function of n_{2D} for monolayer MoS_2 and other semiconductors in the literature (Methods). The black solid line represents the quantum limit for R_c. **e**, Benchmark of monolayer MoS_2 FETs I_{on} at V_{ds} = 1 V in the literature (Methods). The yellow, blue and pink ellipses represent the performance of high-performance (HP, solid symbols) and low-power (LP, open symbols) Si planar FET, FinFET and GAAFET, respectively. It is noted that the data (red pentagram symbols) for Sb (01$\bar{1}$2)-contacted MoS_2 FETs come from 587 devices with different L_c, including 1.5 µm (83 devices), 1 µm (83), 800 nm (83), 600 nm (82), 400 nm (82), 200 nm (80), 100 nm (80), 60 nm (5), 40 nm (5) and 20 nm (4). For better clarity, the average I_{on} (red pentagrams) and standard deviation (error bars) for each L_c are plotted to avoid too many data points. **f**, Benchmark of the delay time of Sb (01$\bar{1}$2)–MoS_2 FETs with Si planar FET, FinFET and GAAFET. All data for MoS_2 FETs are evaluated at V_{ds} = 1 V. The blue and red solid lines represent the fitting of the experimental data points for Si planar HP FET and Sb (01$\bar{1}$2)–MoS_2 FETs, respectively. Gra, graphene; h-BN, hexagonal boron nitride; V_{dd}, operating voltage; L_g, gate length; UHF, ultra-high vacuum. The pink dotted line is the projected result assuming R_c = 42 Ω µm.

(Extended Data Fig. 3c,d). The STEM revealed a pristine and intimate contact between the crystalline Sb and MoS_2 without metal-induced defects. Low-temperature photoluminescence spectroscopy also revealed no defect-related emission after Sb deposition (Extended Data Fig. 3a). The vdW distance between the Sb and the sulfur (S) atoms was measured to be about 0.285 nm (Fig. 2d), which was smaller than that in MoS_2–indium[4] and MoS_2–Bi (0001)[7] contacts. The high-resolution STEM image clearly resolved the atomic positions, in good agreement with the theoretical model in Fig. 1. The absence of Sb–S chemical bond formation was confirmed by X-ray photoemission spectroscopy (Extended Data Fig. 3b). We note that the Sb (01$\bar{1}$2) was formed only on top of MoS_2. Figure 2e presents an optical micrograph of patterned MoS_2 on silicon dioxide (SiO_2) substrate, covered by 20-nm Sb. The Sb film showed a clear colour contrast on MoS_2 and SiO_2 owing to the amorphous nature of SiO_2 (Fig. 2b).

Next, we evaluated the electrical properties of the contact by measuring field-effect transistors (FETs) using MoS_2 single crystals as the channel[31] (see Methods for fabrication and measurement details). Figure 3a shows the transfer (drain-to-source current, I_{ds}, versus gate-to-source voltage, V_{gs}) characteristics of a transfer-length-method (TLM) device. Using TLM, R_c and transfer length (L_T) were derived to be 42 Ω µm and 5.1 nm at $n_{2D} = 3 \times 10^{13}$ cm^{-2}, as shown in Fig. 3b. To our knowledge, both values are the lowest reported for TMD materials, and the R_c is about three-times lower than the previous record using Bi (0001)[7]. It is noteworthy that the small L_T ensures an ultra-compact device footprint, which is critical for very-large-scale integration[32]. Moreover, the small L_T was further corroborated by the negligible on-state current (I_{on}) drop for contact lengths down to about 60 nm (Extended Data Fig. 4g–i). Furthermore, the variable-temperature measurements in Fig. 3c show the temperature-dependent R_c and intrinsic mobility μ_{int} (after eliminating R_c) from 50 K to 400 K. The mobility showed a typical phonon-limited behaviour ($\mu \approx T^{-\gamma}$, where γ is the characteristic exponent of phonon-limited transport and T is the temperature) at high temperature with γ = 1.8, and defect-limited saturation behaviour at low temperature[33]. Remarkably, the R_c was temperature independent in the entire range, suggesting that the cross-junction transport was through tunnelling instead of thermionic emission[14]. This was strong evidence for ohmic contact. The ohmic nature was supported by two additional evidences: (1) the extracted SBH was about −10 meV using the flat-band model[7,18] (Extended Data Fig. 4a–c) and (2) the output (I_{ds} versus drain-to-source voltage, V_{ds}) curves maintained excellent linearity at 50 K (Extended Data Fig. 4c).

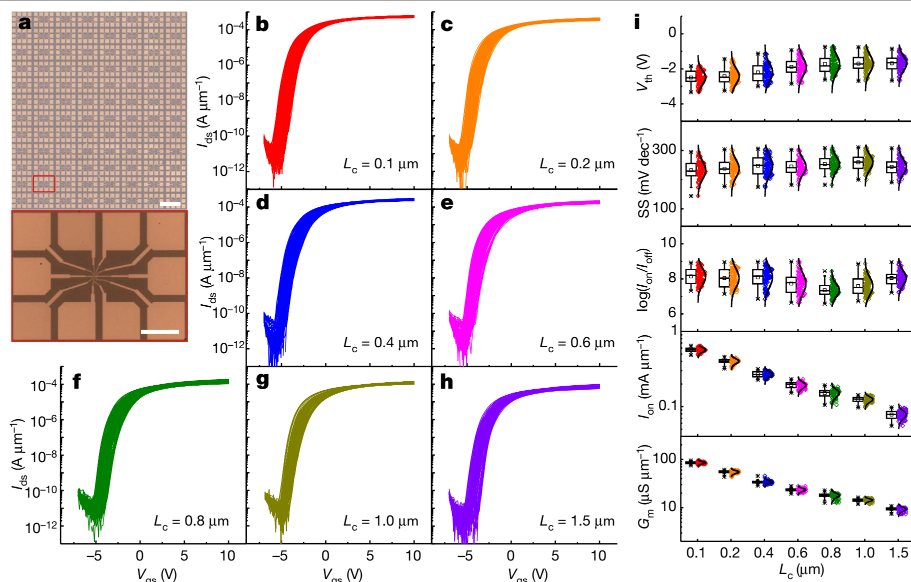

Fig. 5 | Variability of Sb (01$\bar{1}$2)–MoS_2 FETs. a, Top: optical microscope image of TLM arrays fabricated on HfO_2/Si substrate. Scale bar, 400 μm. Bottom: magnified view of a TLM structure. Scale bar, 70 μm. **b**–**h**, Transfer characteristics of MoS_2 FETs with channel lengths of 0.1 μm (**b**), 0.2 μm (**c**), 0.4 μm (**d**), 0.6 μm (**e**), 0.8 μm (**f**), 1.0 μm (**g**) and 1.5 μm (**h**) under V_{ds} = 1 V. **i**, Boxplots with Gaussian fitting of key device metrics, including V_{th}, SS, on/off ratio, G_m and I_{on}. The colour of the symbols corresponds to the channel length in **b**–**h**. For each group of data, the boxplot statistics and Gaussian fitting were performed and meaningful statistical data were obtained, including mean (square symbols), standard deviation, lower quartile (25%), median (50%), upper quartile (75%), interquartile range (25–75%), and maximum and minimum (cross symbols).

To demonstrate the advantage of the Sb (01$\bar{1}$2) contact, we fabricated control TLM devices using an Sb (0001) contact (Fig. 2b). Figure 3d,e shows the statistics of R_c and L_T derived from 156 TLM devices (115 high temperature and 41 ambient temperature). The average R_c of the Sb (01$\bar{1}$2) contact was 209 ± 100 Ω μm, which was 3.47-times lower than the Sb (0001) counterpart. A similar trend was observed for L_T. The high confidence of R_c was supported by the standard deviation σ and correlation coefficient R^2 from the fitting process as well as the TLM structure extending to sub-100-nm channel length, L_c (Extended Data Fig. 5). We note that the improvement using the Sb (01$\bar{1}$2) contact was not due to the MoS_2 quality, as supported by nearly the same average mobility for the two cases (Fig. 3f). In addition, variable-temperature measurements revealed a small but positive SBH of about 20 meV for the Sb (0001) contact (Extended Data Fig. 4d–f), consistent with the recent results from the Taiwan Semiconductor Manufacturing Company (TSMC)[9]. Owing to the improved contacts of Sb (01$\bar{1}$2), the FETs delivered an average 38%-higher I_{on} at 100-nm L_c (Extended Data Fig. 6).

Besides electrical performance, the stability of the contact is also critical to applications. The stability of Bi is poor owing to its low melting point below 300 °C, which posts severe limits in back-end processes. In contrast, the melting point of Sb is above 600 °C. To this end, we studied the device stability at 125 °C (which is the highest standard for electronic products[34]) in a nitrogen environment as shown in Extended Data Fig. 7. No obvious degradation of I_{on}, threshold voltage (V_{th}) and subthreshold swing (SS) was observed during 24 h for the Sb contact. In contrast, the I_{on} of Bi-contact devices decreased by 41% under the same conditions. The excellent stability of the Sb (01$\bar{1}$2) contact also ensures that the devices can work reliably in the high-current regime, as shown in the following.

To fully determine the potential of the Sb (01$\bar{1}$2) contact, we fabricated scaled MoS_2 FETs with sub-50-nm L_c (Fig. 4a). Figure 4b,c shows the I_{ds}–V_{gs} and I_{ds}–V_{ds} characteristics of a representative device with $L_c \approx$ 20 nm (more device data are shown in Extended Data Fig. 8). The device showed excellent short-channel immunity, with an on/off ratio over 10^8, an SS of about 180 mV dec^{-1} and negligible drain-induced barrier lowering. More importantly, the device readily reached current saturation at V_{ds} = 1 V as evident from both transfer and output characteristics. The I_{on} (1.23 mA μm^{-1}) was 44.7% and 104% higher than short-channel devices with Bi (0001) and Sb (0001) contacts, respectively, under the same drain bias[7,9]. Both the saturation voltage and I_{on} were unprecedented in TMDs owing to the improved contacts.

TMD FETs are difficult to remove heat from, because the thin TMD and the vdW gaps around it are highly thermally resistive. As such, self-heating can lead to very high temperatures in the channel, degrading mobility and current, or leading to device failure. The high input power (>1 mW μm^{-1}) in direct-current (d.c.) measurements cause significant self-heating, as indicated by the negative differential resistance at V_{ds} > 1 V (Fig. 4c). To estimate the steady-state temperature distribution of this device at its maximum power, we used finite-element-method simulations[35]. The temperature distribution along the drain–source direction is shown in Extended Data Fig. 9. For plausible ranges of material and interface thermal properties, we found peak temperature rising above ambient of 630 ± 150 K and 38 ± 20 K in the MoS_2 channel and the contacts, respectively. It is noted that the contacts remain significantly cooler than MoS_2, as they are relatively thick and thermally conductive. The large uncertainties in the temperature are mainly owing to the unknown thermal boundary resistance between MoS_2 and Sb (01$\bar{1}$2), which is a subject of future research. To probe the intrinsic limits of device I_{on}, we used pulse measurements with 160-ns pulses (Methods). At V_{ds} = 1 V (1.5 V), the pulsed I_{on} was increased to 1.44 mA μm^{-1} (1.54 mA μm^{-1}), accompanied by higher saturation voltage. The boost of I_{on} under pulse measurements was attributed to the combined effects of reduced self-heating and hot-electron charge trapping[36].

We next benchmarked our device performance with existing TMDs and Si complementary metal–oxide–semiconductor (CMOS) technologies. We first summarized the R_c of various materials in Fig. 4d. It was apparent that our R_c was not only one of the lowest among TMDs, but also lower than covalently bonded contacts in Si and compound semiconductors[3]. At high n_{2D}, the R_c was within a factor of two from the quantum limit[3]. The reduced R_c led to a significant boost of I_{on} under

aggressively scaled V_{ds} = 1 V (Fig. 4e). The I_{on} under d.c. and pulse conditions was 44.7% and 68.8% higher than the previous record in monolayer TMDs[7]. More importantly, our devices delivered similar I_{on} with high-performance planar Si CMOS and superior I_{on} than fin-shaped FET (FinFET) and gate-all-round FET (GAAFET) technologies[37,38], and simultaneously showed immunity to short-channel effects owing to the sub-1-nm channel thickness. We further benchmark with Si technologies by comparing the intrinsic gate delay ($\tau = CV_{ds}/I_{on}$, where C is the gate capacitance)[39]. As shown in Fig. 4f, the intrinsic gate delay is 74 fs for 20-nm MoS_2 FETs, which is faster than Si planar devices and FinFETs by 6.9 times and 15.7 times, respectively[37–39]. The solid red line shows the fitting of experimental data using R_c = 240 Ω µm, projecting an intrinsic gate delay of 20 fs at 5-nm L_c. This is an order of magnitude lower than the International Roadmap for Devices and Systems (IRDS) target for 2028[37]. By using the lowest R_c = 42 Ω µm obtained in this work, we project an intrinsic delay of 3.6 fs at 5-nm L_c.

To assess the suitability of Sb (01$\bar{1}$2) contacts for large-scale integration, we fabricated TLM arrays and examined the variability of key device performances (Fig. 5). Figure 5b–h shows the I_{ds}–V_{gs} characteristics of 573 FETs from 96 TLM structures with L_c ranging from 0.1 µm to 1.5 µm. The variability of V_{th}, SS, on/off ratio, I_{on} and transconductance (G_m) as a function of L_c are summarized in Fig. 5i and Extended Data Table 1 (see Methods for details). On the basis of these data, several important conclusions can be drawn. (1) We did not observe a significant change of variability as a function of L_c. (2) Upon scaling to 100 nm, the SS and on/off ratio did not degrade, but a slight negative shift of V_{th} was observed owing to the short-channel effect (this was not obvious for individual devices). However, the V_{th} shift could be reduced by scaling the effective oxide thickness together with L_c. (3) Both I_{on} and G_m were increased by nearly an order of magnitude upon scaling. The boost of on-state performance from 200-nm L_c to 100-nm L_c suggested that the devices were still not contact-limited, further substantiating the low R_c. Extended Data Table 1 summarizes the variability data and compares with the existing literature on TMDs.

In conclusion, we overcame the inherent vdW gap and realized near-quantum-limit electrical contact between MoS_2 and semi-metallic Sb (01$\bar{1}$2) by hybridization of M–S energy bands at the Fermi energy. The R_c surpassed that of covalently bonded M–S contacts and reached as low as 42 Ω µm. Short-channel MoS_2 FETs delivered a high I_{on} of 1.23 mA µm^{-1} (1.54 mA µm^{-1}) under d.c. (pulse) measurements, an on/off ratio over 10^8 and an intrinsic delay of 74 fs. These performances outperformed equivalent Si CMOS technologies and satisfied the 2028 roadmap target. Besides n-type MoS_2, we also demonstrated a low R_c in ambipolar tungsten diselenide (WSe_2) devices (Extended Data Fig. 10), suggesting that Sb (01$\bar{1}$2) may be a universal contact technology for TMD-based electronics beyond Si.

Online content

Any methods, additional references, Nature Portfolio reporting summaries, source data, extended data, supplementary information, acknowledgements, peer review information; details of author contributions and competing interests; and statements of data and code availability are available at https://doi.org/10.1038/s41586-022-05431-4.

1. Akinwande, D. et al. Graphene and two-dimensional materials for silicon technology. *Nature* **573**, 507–518 (2019).
2. Ahmed, Z. et al. Introducing 2D-FETs in device scaling roadmap using DTCO. *In 2020 IEEE International Electron Devices Meeting* 22.5.1–22.5.4 (IEEE, 2020); https://doi.org/10.1109/Iedm13553.2020.9371906.
3. Wang, Y. & Chhowalla, M. Making clean electrical contacts on 2D transition metal dichalcogenides. *Nat. Rev. Phys.* **4**, 101–112 (2022).
4. Wang, Y. et al. Van der Waals contacts between three-dimensional metals and two-dimensional semiconductors. *Nature* **568**, 70–74 (2019).
5. Kappera, R. et al. Phase-engineered low-resistance contacts for ultrathin MoS_2 transistors. *Nat. Mater.* **13**, 1128–1134 (2014).
6. Liu, Y. et al. Approaching the Schottky–Mott limit in van der Waals metal-semiconductor junctions. *Nature* **557**, 696–700 (2018).
7. Shen, P. C. et al. Ultralow contact resistance between semimetal and monolayer semiconductors. *Nature* **593**, 211–217 (2021).
8. English, C. D., Shine, G., Dorgan, V. E., Saraswat, K. C. & Pop, E. Improved contacts to MoS_2 transistors by ultra-high vacuum metal deposition. *Nano Lett.* **16**, 3824–3830 (2016).
9. Chou., A.-S. et al. Antimony semimetal contact with enhanced thermal stability for high performance 2D electronics. In *2021 IEEE International Electron Devices Meeting* 7.2.1–7.2.4 (IEEE, 2021); https://doi.org/10.1109/IEDM19574.2021.9720608.
10. O'Brien, K. P., Penumatcha, C. J. D. A. & Maxey, K. Advancing 2D monolayer CMOS through contact, channel and interface engineering. In *2021 IEEE International Electron Devices Meeting* 7.1.1–7.1.4 (IEEE, 2021); https://doi.org/10.1109/IEDM19574.2021.9720651.
11. Schulman, D. S., Arnold, A. J. & Das, S. Contact engineering for 2D materials and devices. *Chem. Soc. Rev.* **47**, 3037–3058 (2018).
12. Das, S. et al. Transistors based on two-dimensional materials for future integrated circuits. *Nat. Electron.* **4**, 786–799 (2021).
13. Lanza, M., Smets, Q., Huyghebaert, C. & Li, L. J. Yield, variability, reliability, and stability of two-dimensional materials based solid-state electronic devices. *Nat. Commun.* **11**, 5689 (2020).
14. Sze, S. M., Li, Y. & Ng, K. K. *Physics of Semiconductor Devices* (Wiley, 2021).
15. Landauer, R. Spatial variation of currents and fields due to localized scatterers in metallic conduction. *IBM J. Res. Dev.* **1**, 223–231 (1957).
16. Jain, A. et al. One-dimensional edge contacts to a monolayer semiconductor. *Nano Lett.* **19**, 6914–6923 (2019).
17. Cheng, Z. et al. Immunity to contact scaling in MoS_2 transistors using in situ edge contacts. *Nano Lett.* **19**, 5077–5085 (2019).
18. Das, S., Chen, H. Y., Penumatcha, A. V. & Appenzeller, J. High performance multilayer MoS_2 transistors with scandium contacts. *Nano Lett.* **13**, 100–105 (2013).
19. Jung, Y. et al. Transferred via contacts as a platform for ideal two-dimensional transistors. *Nat. Electron.* **2**, 187–194 (2019).
20. Fang, H. et al. Degenerate n-doping of few-layer transition metal dichalcogenides by potassium. *Nano Lett.* **13**, 1991–1995 (2013).
21. McClellan, C. J., Yalon, E., Smithe, K. K. H., Suryavanshi, S. V. & Pop, E. High current density in monolayer MoS_2 doped by AlO_x. *ACS Nano* **15**, 1587–1596 (2021).
22. Cui, X. et al. Low-temperature ohmic contact to monolayer MoS_2 by van der Waals bonded Co/h-BN electrodes. *Nano Lett.* **17**, 4781–4786 (2017).
23. Wang, J. et al. High mobility MoS_2 transistor with low Schottky barrier contact by using atomic thick h-BN as a tunneling layer. *Adv. Mater.* **28**, 8302–8308 (2016).
24. Chou, A. S. et al. High on-state current in chemical vapor deposited monolayer MoS_2 nFETs with Sn ohmic contacts. *IEEE Electron Device Lett.* **42**, 272–275 (2021).
25. Kang, J. H., Liu, W., Sarkar, D., Jena, D. & Banerjee, K. Computational study of metal contacts to monolayer transition-metal dichalcogenide semiconductors. *Phys Rev. X* **4**, 031005 (2014).
26. Louie, S. G. & Cohen, M. L. Electronic-structure of a metal–semiconductor interface. *Phys. Rev. B* **13**, 2461–2469 (1976).
27. Qiu, H. et al. Hopping transport through defect-induced localized states in molybdenum disulphide. *Nat. Commun.* **4**, 2642 (2013).
28. Jones, A. J. H. et al. Visualizing band structure hybridization and superlattice effects in twisted MoS_2/WS_2 heterobilayers. *2D Mater.* https://doi.org/10.1088/2053-1583/ac3feb (2021).
29. Ji, J. et al. Two-dimensional antimonene single crystals grown by van der Waals epitaxy. *Nat. Commun.* **7**, 13352 (2016).
30. Chen, H. A. et al. Single-crystal antimonene films prepared by molecular beam epitaxy: selective growth and contact resistance reduction of the 2D material heterostructure. *ACS Appl. Mater. Interfaces* **10**, 15058–15064 (2018).
31. Li, T. et al. Epitaxial growth of wafer-scale molybdenum disulfide semiconductor single crystals on sapphire. *Nat. Nanotechnol.* **16**, 1201–1207 (2021).
32. Smets, Q. et al. Ultra-scaled MOCVD MoS_2 MOSFETs with 42 nm contact pitch and 250 µA/µm drain current. In *2019 IEEE International Electron Devices Meeting* 23.2.1–23.2.4 (IEEE, 2019); https://doi.org/10.1109/IEDM19573.2019.8993650.
33. Cui, X. et al. Multi-terminal transport measurements of MoS_2 using a van der Waals heterostructure device platform. *Nat. Nanotechnol.* **10**, 534–540 (2015).
34. *Commercial and Industrial-Grade Products* White Paper CTWP011 (Cactus Technology, 2019).
35. Wu, R. et al. Filling the gap: thermal properties and device applications of graphene. *Sci. China Inf. Sci.* **64**, 140401 (2021).
36. Nathawat, J. et al. Transient hot-carrier dynamics and intrinsic velocity saturation in monolayer MoS_2. *Phys. Rev. Mater.* **4**, 014002 (2020).
37. *International Roadmap for Devices and Systems* (IRDS, 2020); https://irds.ieee.org/
38. *International Technology Roadmap for Semiconductors* (ITRS, 2015); https://www.semiconductors.org/resources/2015-international-technology-roadmap-for-semiconductors-itrs/
39. Chau, R. et al. Benchmarking nanotechnology for high-performance and low-power logic transistor applications. *IEEE Trans. Nanotechnol* **4**, 153–158 (2005).

Publisher's note Springer Nature remains neutral with regard to jurisdictional claims in published maps and institutional affiliations.

Springer Nature or its licensor (e.g. a society or other partner) holds exclusive rights to this article under a publishing agreement with the author(s) or other rightsholder(s); author self-archiving of the accepted manuscript version of this article is solely governed by the terms of such publishing agreement and applicable law.

© The Author(s), under exclusive licence to Springer Nature Limited 2023

Methods

Chemical-vapour-deposition growth and transfer of monolayer MoS_2

We grew single-crystal monolayer MoS_2 on A-axis *c*-plane (C/A) sapphire (0001) substrates with miscut angle α_A ranging from 0.2° to 1° that had undergone 1,000 °C annealing for 4 h as described in our previous work[31]. The transfer of MoS_2 was done by a polymer-based transfer method. Poly(methyl methacrylate) (PMMA; Allresist A4, 950K) was spin-coated on the MoS_2/sapphire substrate at 2,000 r.p.m. After baking at 150 °C to evaporate solvent completely, a thermal release tape (TRT) was laminated and the PMMA/MoS_2 was gently peeled off the sapphire substrate in deionized water. The TRT/PMMA/MoS_2 stack was transferred onto the target substrate and baked at 120 °C to release the TRT.

Chemical-vapour-deposition growth of monolayer WSe_2

We grew monolayer WSe_2 on 100-nm SiN_x/Si substrate using a chemical-vapour-deposition tube furnace with a reverse-flow reactor. An alumina boat loaded with WSe_2 (Alfa Aesar, 99.98%) powder was placed into the heating zone of a quartz tube, and the substrate was placed on the alumina boat and placed in the variable-temperature zone. The chemical-vapour-deposition growth process was carried out at 1,180 °C under ambient pressure with a reverse argon gas flow of 80 standard cubic centimetres per minute. Once the desired growth temperature was reached, the chemical vapour source was carried downstream under a forward argon gas flow of 80 standard cubic centimetres for a growth period of 4 min. After the growth, the furnace was cooled naturally.

Transistor fabrication and measurement

Monolayer MoS_2 film was transferred onto hafnium oxide (HfO_2)/highly doped Si substrate using the PMMA-assisted transfer followed by channel isolation through electron beam lithography and dry etching by O_2. After removing PMMA by acetone and *N*-methyl-2-pyrrolidone (NMP), electron beam lithography was used to define the source and drain contacts followed by electron beam evaporation of 20-nm Sb/30-nm Au and lift-off. We controlled the substrate temperature during electron beam evaporation through infrared heating and adjusting the cooling water flow rate. The substrate temperature was measured using the surface temperature indicating strips. Notably, the Sb $(01\bar{1}2)$ contact did not require any thermal annealing after device fabrication, which made this technology back-end-of-line compatible with CMOS. WSe_2 FETs were fabricated on in-situ SiNx/Si substrate by the same methods without transfer process.

Electrical measurements were carried out by Keithley 4200 semiconductor parameter analyser in a closed-cycle cryogenic probe station with a base pressure of about 10^{-6} torr. Pulse testing was performed using a Keithley 4200 pulse measurement unit in conjunction with model 4225-RPM remote amplifier. During the pulse measurement, a synchronous pulse voltage sequence was applied to the drain and gate electrodes, the minimum pulse width can be as low as 160 ns and the voltage duty cycle was 10 times. To reduce parasitic effects during pulse measurement, all the cables were shortened as much as possible. The data on the MoS_2 FETs shown in Fig. 4d,e are from refs. [3,4,7,9,10,17,21,22,24,31,37,38,40–48].

Characterization

XRD was performed on a Bruker D8 Discover system. AFM was performed by an Asylum Cypher S system. Raman and photoluminescence spectroscopy were carried out by a home-built system equipped with 488-nm laser excitation and Princeton Instruments SP-2500 spectrometer. X-ray photoemission spectroscopy (PHI 5000 VersaProbe Scanning XPS Microprobe with a monochromatized Al Kα excitation source) was performed with calibration to the chemical state of C–C of adventitious carbon at 284.8 eV. Cross-section TEM samples were fabricated using an FEI Helios 600i dual-beam focused ion beam (FIB) system. A tungsten protection layer was in situ deposited before FIB bombardment, followed by etching the surrounding area to form the lamella using a 30-kV acceleration voltage and a 21-nA gallium ion beam. The target lamella was exfoliated from the original substrate and transferred to TEM half grid inside the FIB chamber. HAADF-STEM characterization was acquired on a FEI Titan G2 60–300 aberration-corrected S/TEM microscope with an acceleration voltage of 300 kV.

DFT calculations

First-principles DFT calculations were performed by using the Vienna Ab initio Simulation Package (VASP 5.4)[49] with the exchange-correlation functional based on Perdew–Burke–Ernzerhof[50] generalized gradient approximation. The projected augmented wave potentials was adopted to describe the interactions between valence electrons and ion cores[51]. The Grimme's DFT-D3 scheme was employed to include the vdW interactions[52]. A slab model stacked with monolayer TMDs and three-layer semi-metal (Sb or Bi) (0001)/$(01\bar{1}2)$ plane was used to simulate the MoS_2–Sb contact. The supercells of the semi-metal (0001)/$(01\bar{1}2)$ surfaces and TMDs were carefully built to ensure a lattice mismatch smaller than 3%, where a vacuum space of >15 Å was added to separate images along *c* direction of the supercells. All structures were fully relaxed until the maximum force component acting on each atom was less than 0.02 eV $Å^{-1}$ with an energy convergence criterion of 10^{-4} eV and an kinetic energy cut-off of 400 eV. Considering the very large systems simulated in this work, a *k*-spacing of <0.04 $Å^{-1}$ was used for the structural relaxation of metal (Sb (0001), Sb $(01\bar{1}2)$, Bi(0001) and Bi $(01\bar{1}2)$)–TMD (MoS_2, $MoSe_2$, WS_2 and WSe_2) contacts. For the static electronic structure calculations, the Brillouin zone integrations were sampled on a *k*-spacing of <0.01 $Å^{-1}$ for semi-metal–TMD contacts, respectively. The dipole correction along the *c* axis of supercell was considered in all DFT calculations as well. The electrostatic potential profiles of Sb $(01\bar{1}2)$–MoS_2 and Sb (0001)–MoS_2 contacts along the vertical direction were calculated using Poisson's equation. The real-space band diagrams and the LDDOSs of the device composed of monolayer MoS_2 and double-ended Sb $(01\bar{1}2)$ electrodes without doping (zero bias) and with electron doping (similar to high gate bias) were simulated by using the DFT method.

Data availability

Source data are provided with this paper.

40. Guimaraes, M. H. et al. Atomically thin ohmic edge contacts between two-dimensional materials. *ACS Nano* **10**, 6392–6399 (2016).
41. Smithe, K. K. H., English, C. D., Suryavanshi, S. V. & Pop, E. Intrinsic electrical transport and performance projections of synthetic monolayer MoS_2 devices. *2D Mater.* https://doi.org/10.1088/2053-1583/4/1/011009 (2016).
42. Smithe, K. K. H., Suryavanshi, S. V., Munoz Rojo, M., Tedjarati, A. D. & Pop, E. Low variability in synthetic monolayer MoS_2 devices. *ACS Nano* **11**, 8456–8463 (2017).
43. Zhu, Y. et al. Monolayer molybdenum disulfide transistors with single-atom-thick gates. *Nano Lett.* **18**, 3807–3813 (2018).
44. Kumar, A. et al. Sub-200 Ω·μm alloyed contacts to synthetic monolayer MoS_2. In *2021 IEEE International Electron Devices Meeting* 7.3.1–7.3.4 (IEEE, 2021); https://doi.org/10.1109/IEDM19574.2021.9720609.
45. Somvanshi, D. et al. Nature of carrier injection in metal/2D-semiconductor interface and its implications for the limits of contact resistance. *Phys. Rev. B* **96**, 205423 (2017).
46. Daus, A. et al. High-performance flexible nanoscale transistors based on transition metal dichalcogenides. *Nat. Electron.* **4**, 495–501 (2021).
47. Lembke, D. & Kis, A. Breakdown of high-performance monolayer MoS_2 transistors. *ACS Nano* **6**, 10070–10075 (2012).
48. Sanne, A. et al. Radio frequency transistors and circuits based on CVD MoS_2. *Nano Lett.* **15**, 5039–5045 (2015).
49. Kresse, G. & Furthmuller, J. Efficient iterative schemes for ab initio total-energy calculations using a plane-wave basis set. *Phys. Rev. B* **54**, 11169–11186 (1996).
50. Perdew, J. P., Burke, K. & Ernzerhof, M. Generalized gradient approximation made simple. *Phys. Rev. Lett.* **77**, 3865–3868 (1996).
51. Blochl, P. E. Projector augmented-wave method. *Phys. Rev. B* **50**, 17953–17979 (1994).
52. Jonchiere, R., Seitsonen, A. P., Ferlat, G., Saitta, A. M. & Vuilleumier, R. Van der Waals effects in ab initio water at ambient and supercritical conditions. *J. Chem. Phys.* **135**, 154503 (2011).
53. Sebastian, A., Pendurthi, R., Choudhury, T. H., Redwing, J. M. & Das, S. Benchmarking monolayer MoS_2 and WS_2 field-effect transistors. *Nat. Commun.* **12**, 693 (2021).

Acknowledgements This work was supported by the National Key R&D Program of China (grant numbers 2021YFA0715600, 2022YFB4400100, 2021YFA1500700, 2017YFA0204800 and 2021YFA1202903); the Leading-edge Technology Program of Jiangsu Natural Science Foundation (grant numbers BK20202005 and BK20222007); the National Natural Science Foundation of China (grant numbers T2221003, 61927808, 61734003, 61851401, 91964202, 61861166001, 51861145202, 22033002, 62204113, 62204124, 22222302, 11774153 and 11874199); the China Postdoctoral Science Foundation (grant numbers 2022M711549 and 2022T15036); Jiangsu Funding Program for Excellent Postdoctoral Talent (grant number 2022ZB63); the Natural Science Foundation of Jiangsu Province (grant number BK20220773); the Strategic Priority Research Program of Chinese Academy of Sciences (grant number XDB30000000); the Key Laboratory of Advanced Photonic and Electronic Materials, Collaborative Innovation Center of Solid-State Lighting and Energy-Saving Electronics, and the Fundamental Research Funds for the Central Universities, China.

Author contributions X.W. and Y.S. conceived and supervised the project. W.L., Z.Y., H.N., D.F., Y.X., X.T. and H.Q. contributed to the transistor fabrication, measurements and data analysis. X.G., L.M. and J.W. performed the DFT calculations. W.S. and Y.N. performed the XRD and data analysis. Ç.K. and E.P. performed the thermal analysis. S.G., P.W., T.X. and L.S. performed the TEM and data analysis. Wenfeng Wang, L.L. and T.L. performed the chemical-vapour-deposition growth of MoS_2. J. Li and X.D. performed the chemical-vapour-deposition growth of WSe_2. Wenhui Wang, J. Lu and Z.N. performed the Raman characterization and data analysis. W.L., Z.Y., L.M., J.W. and X.W. co-wrote the manuscript with input from other authors. All authors contributed to discussions.

Competing interests The authors declare no competing interests.

Additional information

Supplementary information The online version contains supplementary material available at https://doi.org/10.1038/s41586-022-05431-4.

Correspondence and requests for materials should be addressed to Yi Shi, Jinlan Wang or Xinran Wang.

Peer review information *Nature* thanks Abhinandan Borah, Hyeon-Jin Shin and the other, anonymous, reviewer(s) for their contribution to the peer review of this work.

Reprints and permissions information is available at http://www.nature.com/reprints.

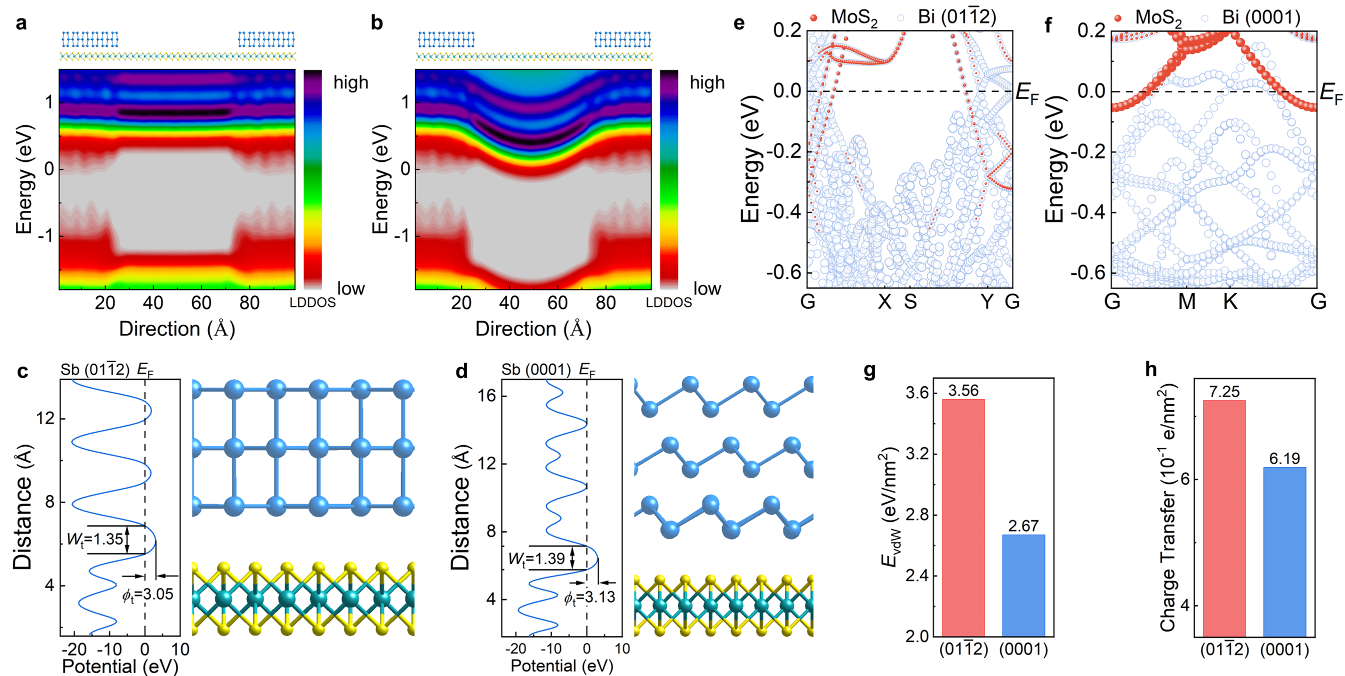

Extended Data Fig. 1 | Electronic properties of Sb/Bi-MoS_2 contacts. **a**, **b**, The simulated band diagram and local device density of states (LDDOS) of the monolayer MoS_2 with double-end Sb (01$\bar{1}$2) electrodes: without electron doping (zero gate bias) (**a**) and with 1.5 electron doping (similar to high gate bias) (**b**). The Fermi level is set to zero. **c**, **d**, Electrostatic potential profiles of Sb (01$\bar{1}$2)-MoS_2 (**c**) and Sb (0001)-MoS_2 (**d**) contacts along the vertical direction, respectively. **e**, **f**, Atomic-projected electronic band structures of Bi (01$\bar{1}$2)-MoS_2 (**e**) and Bi (0001)-MoS_2 (**f**) contacts. **g**, The interfacial vdW interaction between MoS_2 and Bi (01$\bar{1}$2)/Bi (0001). **h**, The charge transfer from Bi (0112)/Bi (0001) to MoS_2 by Bader charge analysis.

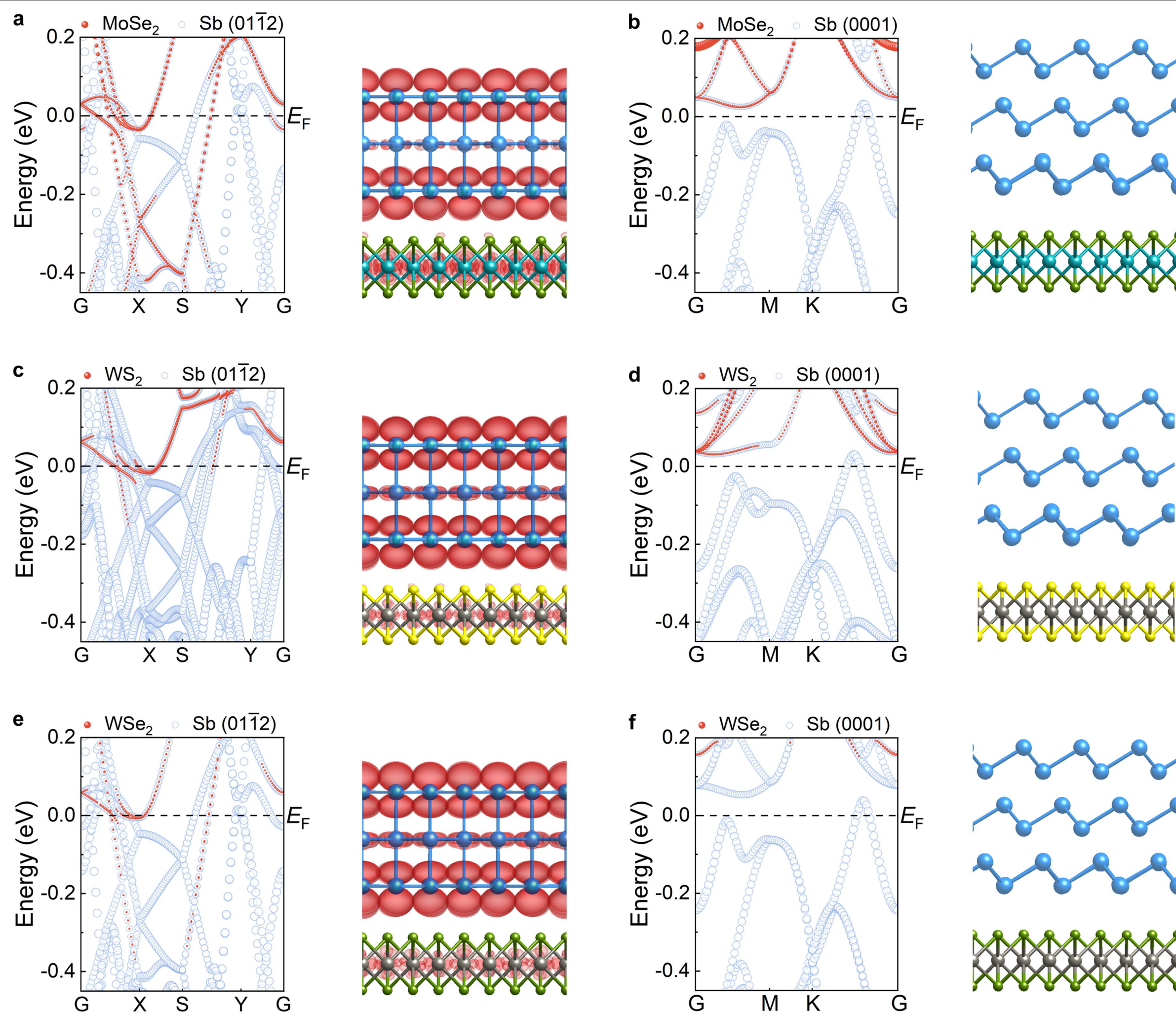

Extended Data Fig. 2 | The atomic-projected electronic band structures and the charge density near E_F of TMDs-Sb contact. a–f, Left panels, atomic-projected electronic band structures (left panel) of $MoSe_2$-Sb (01$\bar{1}$2) (**a**), WS_2-Sb (01$\bar{1}$2) (**c**), WSe_2- Sb (01$\bar{1}$2) (**e**), $MoSe_2$-Sb (0001) (**b**), WS_2-Sb (0001) (**d**) and WSe_2-Sb (0001) (**f**) contacts. Right panels, charge density near E_F of $MoSe_2$-Sb (01$\bar{1}$2) (**a**), WS_2-Sb (01$\bar{1}$2) (**c**), WSe_2- Sb (01$\bar{1}$2) (**e**), $MoSe_2$-Sb (0001) (**b**), WS_2-Sb (0001) (**d**) and WSe_2-Sb (0001) (**f**) contacts. The corresponding isosurface level of the charge density near E_F (right panel) are 1.3×10^{-4} e/$Bohr^3$ for $MoSe_2$-Sb contact (**a**, **b**), 8×10^{-5} e/$Bohr^3$ for WS_2-Sb (**c**, **d**) and WSe_2-Sb (**e**, **f**) contact, respectively.

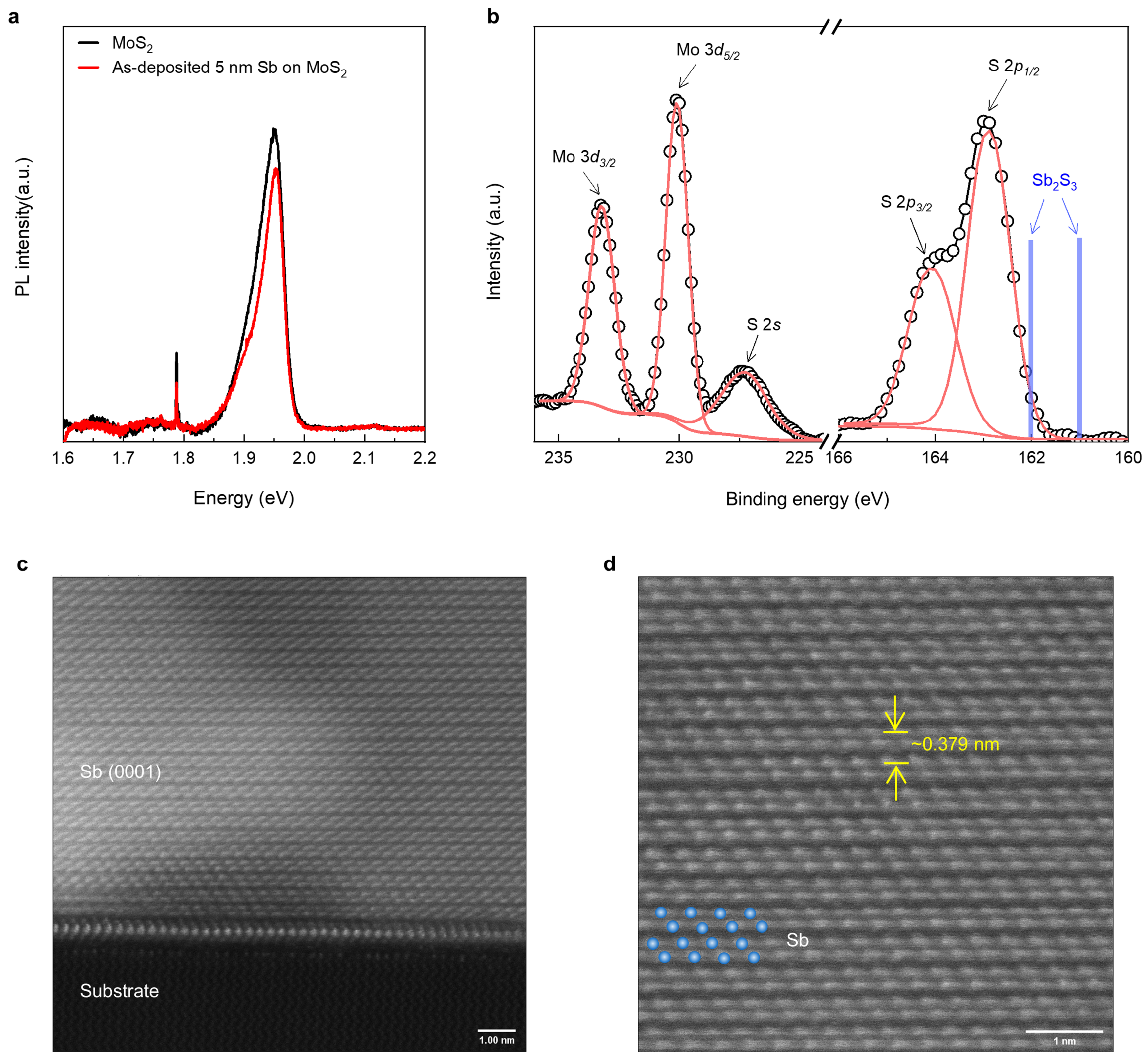

Extended Data Fig. 3 | Optical, chemical and structural characterization of Sb-MoS_2 interface. **a**, The Low-temperature (6 k) PL spectra of. After depositing Sb film, the main exciton peak did not show widening, and no obvious defect-related emissions were observed. This proved that the deposition of Sb was friendly to 2D materials without creating defects. The sharp peak at 1.79 eV was the photoluminescence signal from the sapphire substrate. **b**, High-resolution XPS spectra of 2 nm Sb deposited on monolayer MoS_2/sapphire, where the absence of Sb−S bond signal from Sb_2S_3 indicates no chemical bond formation between Sb and MoS_2. **c**, Cross-section HAADF-STEM image of Sb (0001)-MoS_2 contact. Scale bar, 1 nm. **d**, Zoom-in atomic-resolution image from **c**. The interplane distance was 0.379 nm. Scale bar, 1 nm.

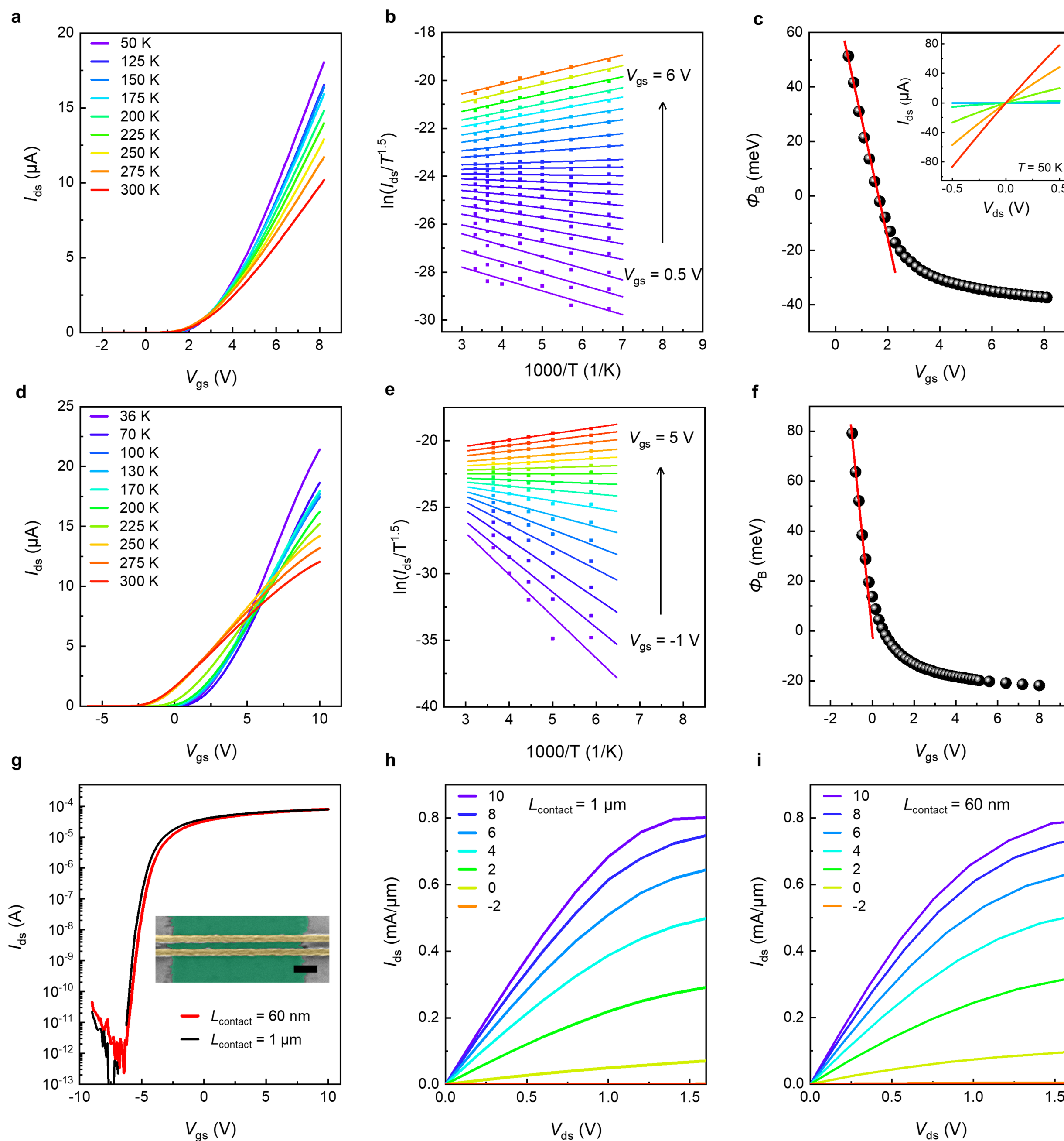

Extended Data Fig. 4 | Schottky barrier extraction and small footprint MoS_2 FETs. **a**, The temperature-dependent I_{ds}-V_{gs} transfer curves of Sb (01$\bar{1}$2)-MoS_2 FET. V_{ds} = 0.1V. **b**, The Arrhenius plot at various gate bias of the same device in **a**. **c**, Gate voltage dependence of the barrier height. The deviation from the linear trend (red solid line) defines the flat band voltage and shows negative Schottky barrier height. Inset shows the linear output curves of the same FET at a low temperature of 50 K with excellent linearity. **d**, The temperature-dependent I_{ds}-V_{gs} transfer curves of Sb (0001)-MoS_2 FET. V_{ds} = 0.1V. **e**, The Arrhenius plot at various gate bias of the same device in **d**. **f**, Gate voltage dependence of the barrier height. The deviation from the linear trend (red solid line) defines the flat band voltage and shows positive Schottky barrier height. **g**, Transfer curves of two MoS_2 FETs with the same L_c = 60 nm but with contact length ($L_{contact}$) of 60 nm and 1 μm. V_{ds} = 0.1 V. Inset is the false-colour SEM image of the device. Scale bar, 200 nm. **h**–**i**, Output curves of the MoS_2 FET with contact length of 1 μm (**h**) and 60 nm (**i**), respectively.

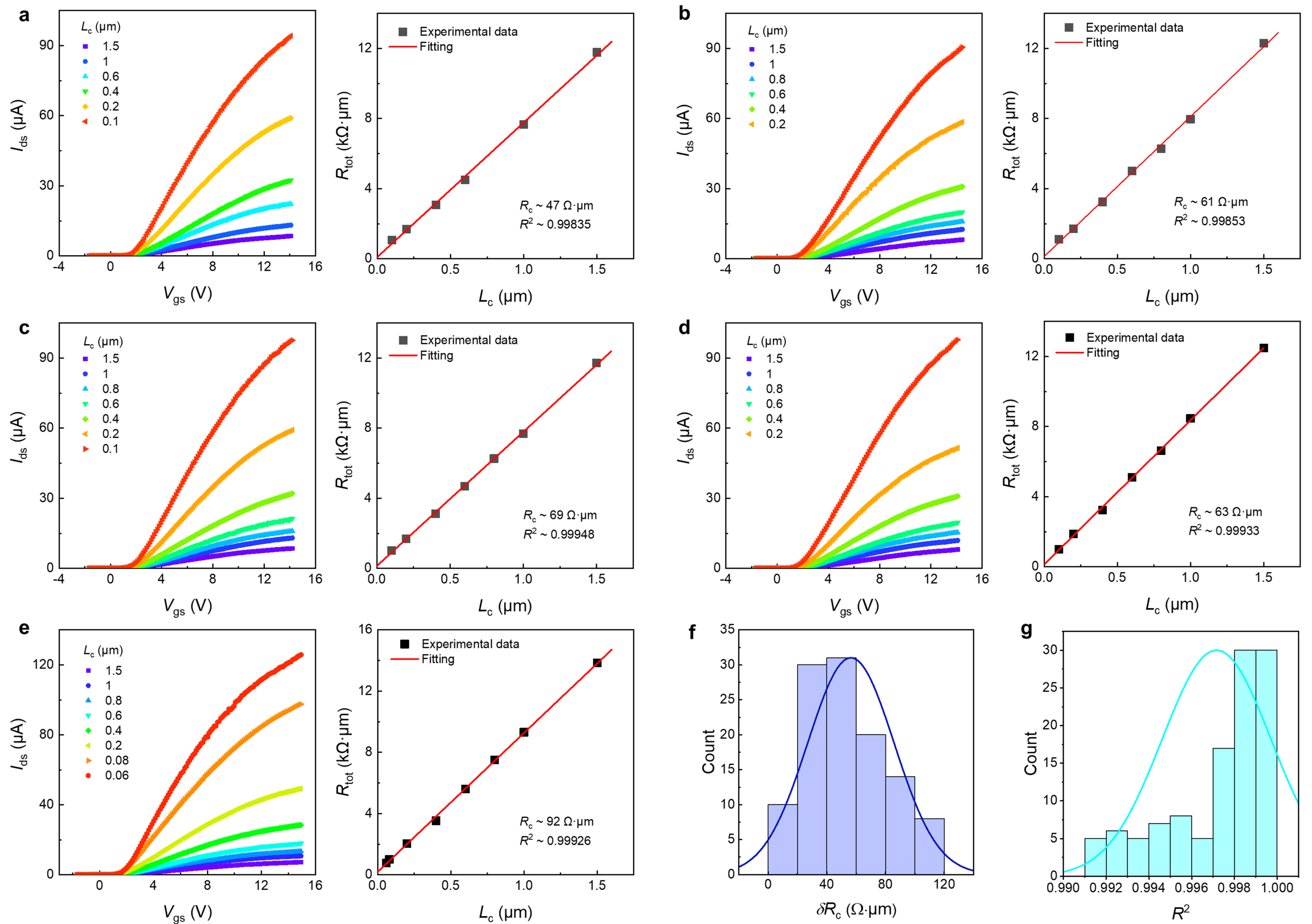

Extended Data Fig. 5 | Extraction of low R_c from TLM devices with Sb (01$\bar{1}$2) -MoS_2. a–e, The left is the transfer curves of TLM devices. V_{ds} = 0.1V, and the right is the plot of R_{tot} versus L_c from the left devices, from which the 2R_c can be extracted from the y-axis intercepts. Symbols are experimental data and lines are linear fits at the right figure. It is noted that TLM in **e** contain 9 devices with L_c equal to 60 nm, 80 nm, 200 nm, 400 nm, 600 nm, 800 nm, 1 μm and 1.5 μm. Ultralow R_c extraction from the TLM devices with sub-100-nm L_c devices further enhances confidence in ohmic contact of Sb (01$\bar{1}$2) -MoS_2 contact. **f**, **g**, Histogram of σ (**a**) and R^2 (**b**) from the linear fitting process of TLM method corresponding to the results of Sb (01$\bar{1}$2)-MoS_2 contact (115 TLMs) in Fig. 3d and e.

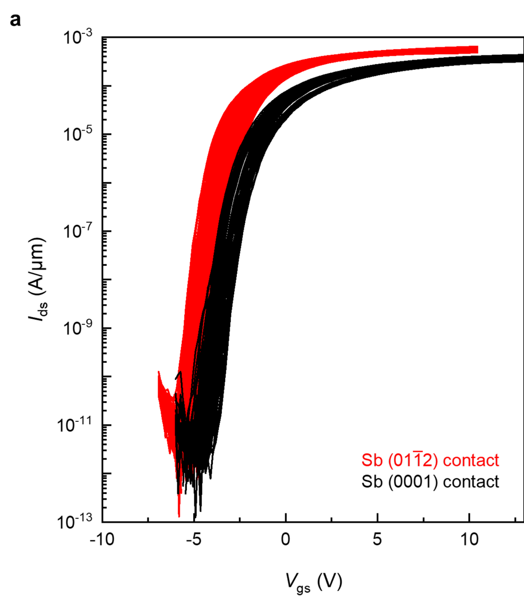

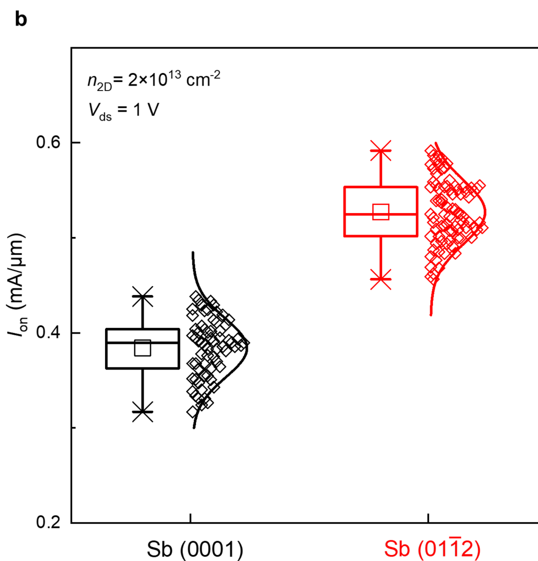

Extended Data Fig. 6 | Comparison of MoS_2 FETs with Sb (0001) and Sb (01$\bar{1}$2) **contacts.** **a**, Transfer characteristics of 145 MoS_2 FETs (65 with Sb (0001) contact (black lines) and 80 with Sb (01$\bar{1}$2) contact (red lines)). L_c = 100 nm, V_{ds} = 1V. **b**, The boxplot with Gaussian fitting of I_{on} at the same carrier density. The mean (square symbols), lower quartile (Q1, 25%), median (Q2, 50%), upper quartile (Q3, 75%), interquartile range (25%-75%) and maximum/minimum (cross symbols) are presented. The I_{on} of Sb (01$\bar{1}$2) contact is significantly improved compared with Sb (0001) contact due to the improvement of R_c.

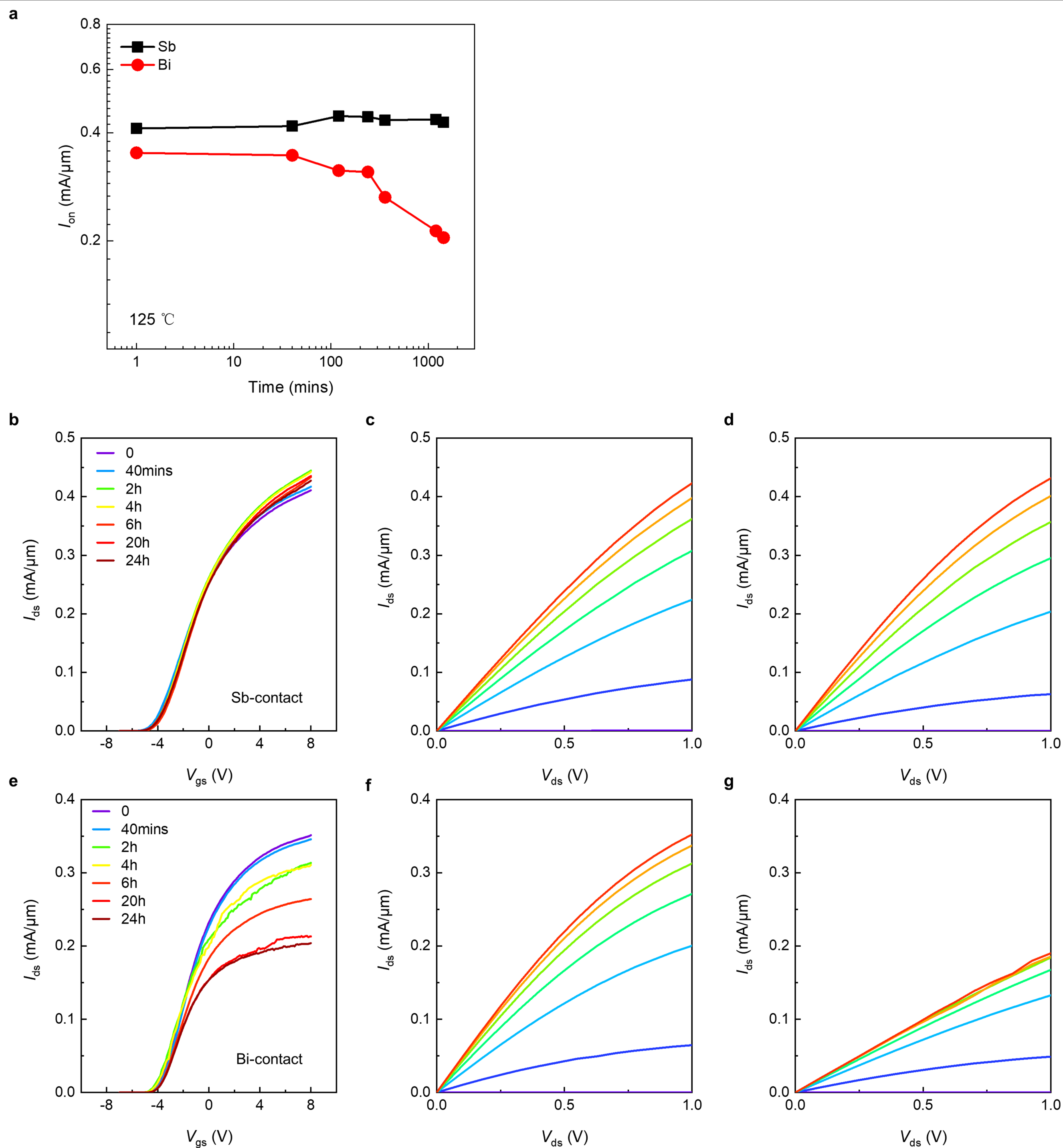

Extended Data Fig. 7 | Stability of Sb (01$\bar{1}$2)**-MoS_2 contact. a**, Thermal stability of I_{on} for Sb and Bi contact measured at different time in 125 °C nitrogen environment. **b**, Transfer characteristics of a typical Sb-contact MoS_2 FET measured L_c = 100 nm, V_{ds} = 1V. **c**, **d**, The output characteristics of the same device in the initial state (**c**) and after 24 h (**d**). From bottom to up, V_{gs} = −2 V to 10 V with 2 V step. **e**, Transfer characteristics of a typical Bi-contact MoS_2 FET measured at different time in 125 °C nitrogen environments. L_c = 100 nm, V_{ds} = 1V. **f**, **g**, The output characteristics of the same device at 125 °C in the initial state (**f**) and after 24 h (**g**). From bottom to up, V_{gs} = −2 V to 10 V with 2 V step.

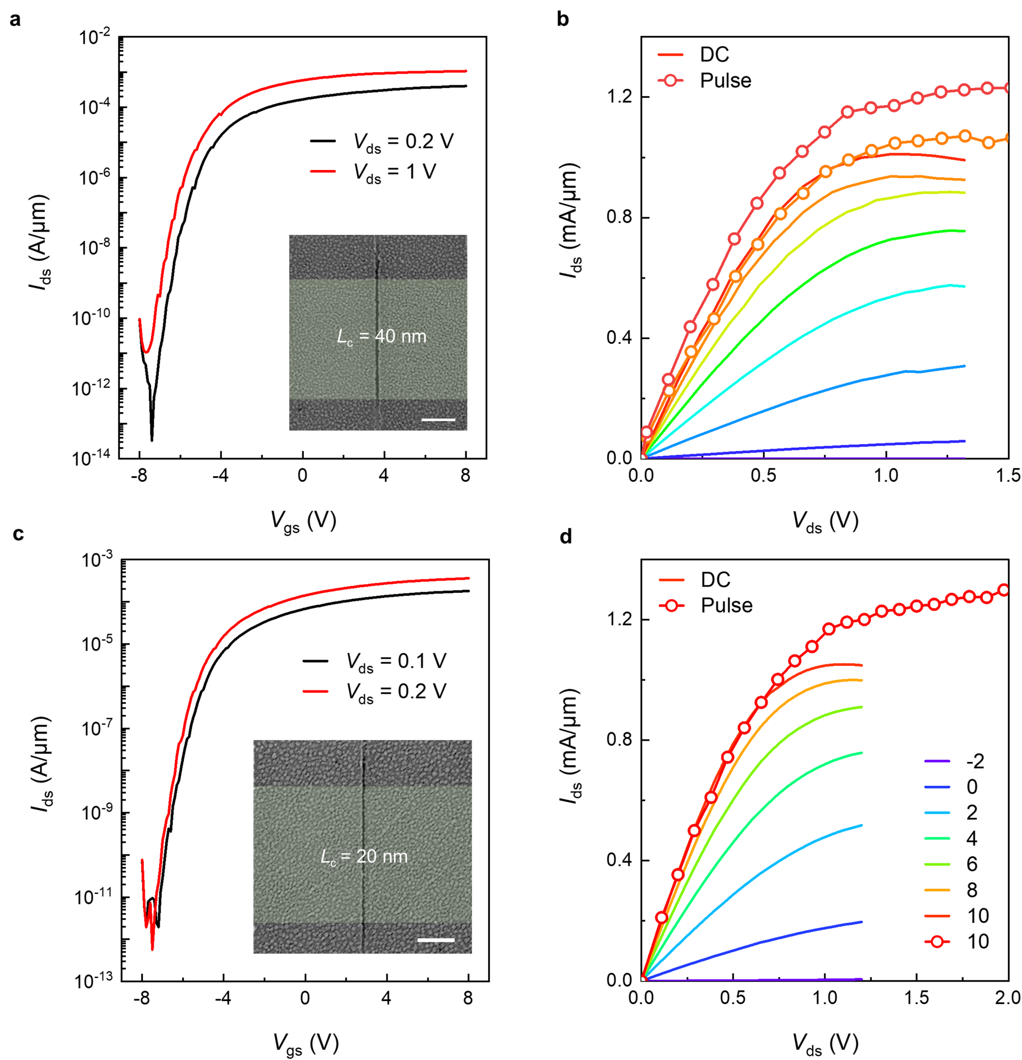

Extended Data Fig. 8 | Short-channel MoS_2 FETs with Sb (01$\bar{1}$2)-contact. **a**, Transfer characteristics of a MoS_2 FET with L_c = 40 nm under V_{ds} = 0.2 V and 1 V. Inset shows the corresponding SEM image. Scale bar, 500 nm. **b**, The output characteristics of the same devices in **a**. From bottom to up, V_{gs} = −2 V to 10 V with 2 V step. The solid and dotted lines are the results of the DC and pulse I-V measurements, respectively. **c**, Transfer characteristics of a MoS_2 FET with L_c = 20 nm under V_{ds} = 0.2 V and 1 V. Inset shows the corresponding SEM image. Scale bar, 500 nm. **d**, The output characteristics of the same devices in **c**. From bottom to up, V_{gs} = −2 V to 10 V with 2 V step. The solid and dotted lines are the results of the DC and pulse I-V measurements, respectively.

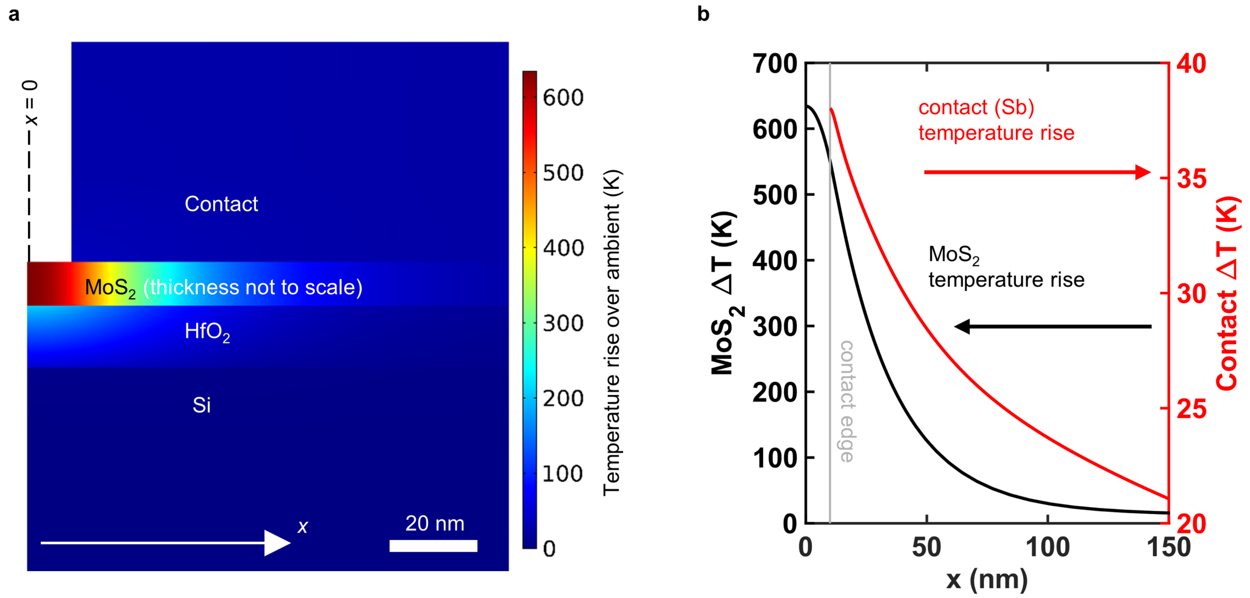

Extended Data Fig. 9 | The steady-state temperature distribution of the short-channel MoS_2 FET in Fig. 4b, c by finite-element method simulation. **a**, Steady-state distribution of temperature rises across the centre cross-section of the device along the current direction, for $V_{ds} = 1$ V and $I_{ds} = 1.23$ mA/μm. Only half of the geometry is shown, $x = 0$ (halfway between the drain and source contacts) serving as the symmetry plane. A contact resistance of 100 Ω·μm is assumed in order to determine the fraction of the power dissipated at the contacts. **b**, The temperature rise above ambient in MoS_2 (black) and the contact just above MoS_2 (red) plotted as a function of position along the direction of current flow.

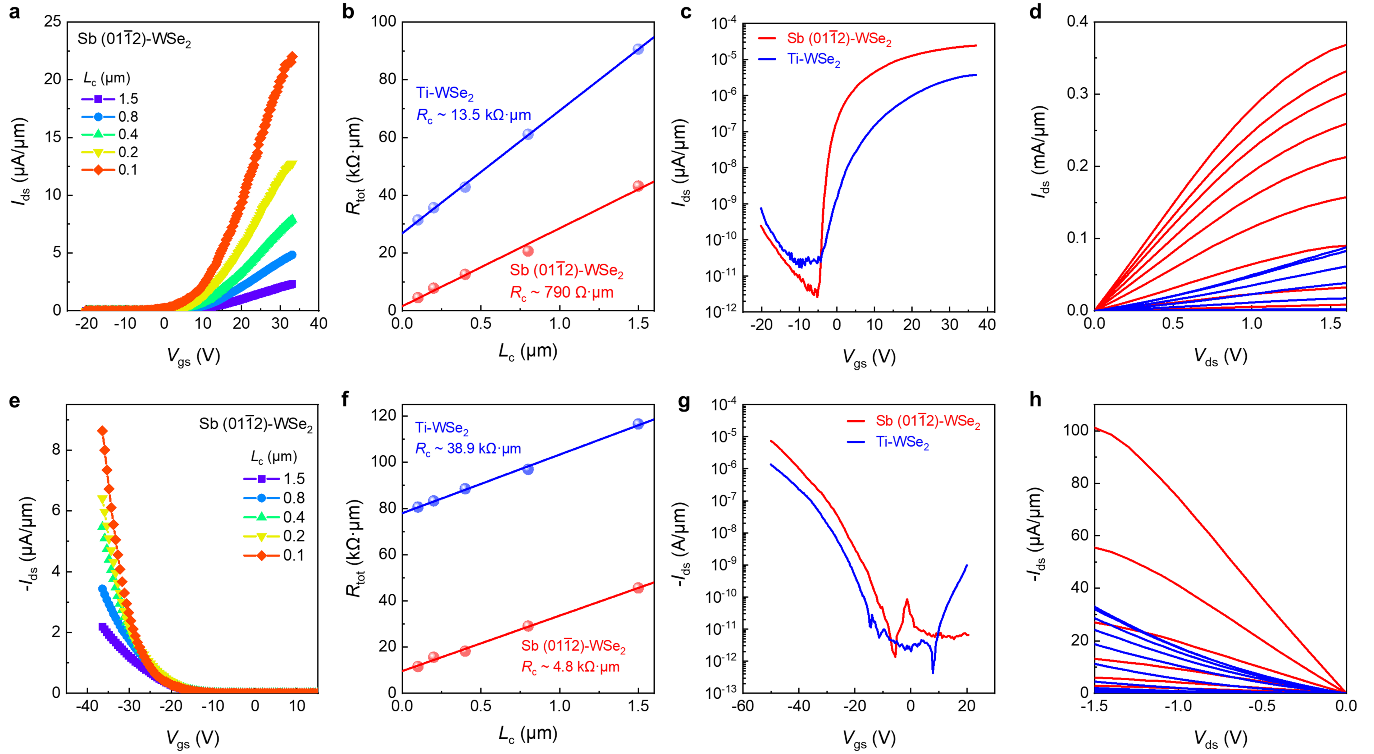

Extended Data Fig. 10 | Ambipolar monolayer WSe$_2$ FETs with Sb (01$\bar{1}$2) **contact. a**, Transfer curves of n-type TLM devices with Sb (01$\bar{1}$2) contact. V_{ds} = 0.1 V. **b**, Plot of R_{tot} versus L_c from n-type TLM devices with Sb (01$\bar{1}$2) contact (red symbols) and Ti contact (blue symbols), from which the 2R_c can be extracted from the y-axis intercepts. Symbols are experimental data and lines are linear fits at **b**. **c**, **d**, Performance comparison of n-type monolayer WSe$_2$ FETs with Sb (01$\bar{1}$2) contact (red) and Ti contact (blue). L_c = 100 nm. **c** shows the transfer curves at V_{ds} = 0.1 V. **d** shows the output curves at V_{gs} from 0 V to 40 V with 4 V step with the same devices at **c**. **e**, Transfer curves of p-type TLM devices with Sb (01$\bar{1}$2) contact. V_{ds} = −0.1 V. **f**, Plot of R_{tot} versus L_c from p-type TLM devices with Sb (01$\bar{1}$2) contact (red symbols) and Ti contact (blue symbols), from which the 2R_c can be extracted from the y-axis intercepts. Symbols are experimental data and lines are linear fits at **f**. **g**, **h**, Performance comparison of p-type monolayer WSe$_2$ FETs with Sb (01$\bar{1}$2) contact (red) and Ti contact (blue). L_c = 100 nm. **g** shows the transfer curves. V_{ds} = −0.1 V. **h** shows the output curves at V_{gs} from 0 V to −50 V with −5 V step with the same devices at **g**.

Extended Data Table 1 | Variability data analysis and benchmark[42,53]

Channel	L_c (μm)	#devices	Dielectric	V_{th} (V)	*SS* (mV/dec)	*Log* (I_{on}/I_{off})	I_{on} (μA/μm)	G_m (μs/μm)	R_c (kΩ·μm)	Ref.
1L MoS_2	0.1	80	14 nm HfO_2	-2.50±0.39	232±30	8.14±0.46	569±40	85±4.8	0.209±0.1	This work
	0.2	80		-2.42±0.44	238±29	8.04±0.53	402±30	55±3.7		
	0.4	82		-2.20±0.50	248±32	8.08±0.56	268±23	34±2.4		
	0.6	82		-1.88±0.51	245±26	7.73±0.57	193±18	23±1.7		
	0.8	83		-1.72±0.52	253±24	7.34±0.36	150±18	18±2.0		
	1	83		-1.70±0.49	259±24	7.58±0.50	124±10	14±1.0		
	1.5	83		-1.68±0.41	245±25	8.04±0.40	78±9.7	9.3±0.9		
1L MoS_2	0.1	17	50 nm Al_2O_3	2.9±0.8	335±115	7.53±0.42	54±13		9.2	[53]
1L WS_2	0.1	22	50 nm Al_2O_3	6.5±0.8	443±66	7.43±0.86	13±8		29.2	[53]
1-2L MoS_2	4-9	200	30 nm SiO_2	-2.36±1.08		5.86±0.25			2.9±0.9	[42]

V_{th} is the threshold voltage of the device, which is extracted by using the linear extrapolation method. SS is the subthreshold swing extracted from the device in the subthreshold region. I_{on} is the drain current when the device is in the 'on' state. log(I_{on}/I_{off}) is the logarithm value of the ratio of the drain currents when the device is in the 'on' and 'off' states, respectively. G_m is the transconductance value of the device at V_{ds}=1V. Missing values are represented by spaces. The results for V_{th}, SS, log(I_{on}/I_{off}), I_{on}, G_m and R_c are all obtained by statistical analysis of many devices (#devices is the statistical number of the devices) and presented as "mean ± standard deviation".